Draft version October 7, 2025
Typeset using LaTeX default style in AASTeX62

Magnetic Amplification of Photoevaporation: Coupled Dynamo and Ohmic Heating in Hot Saturns

Koen Schenck[1] and Howard Chen[1,2]

[1] Department of Aerospace, Physics, and Space Sciences, Florida Institute of Technology, Melbourne, FL 32901
[2] Sellers Exoplanet Environments Collaboration (SEEC), NASA Goddard Space Flight Center, Greenbelt, MD 20771

ABSTRACT

The coupled thermal and mass-loss evolution of close-in gaseous exoplanets is governed by a combination of post-formation processes. For highly irradiated exoplanets ($T_{\rm eq} > 1000$ K), hydrodynamic escape during the high-EUV phases of stellar evolution and Ohmic dissipation from the interaction between ionized winds and planetary magnetic fields both play central roles in shaping their long-term outcomes. Here, we compute time-dependent planetary magnetic fields from convective dynamo scaling and use them to self-consistently evaluate volumetric Ohmic heating in the deep interiors of hot Saturn-mass worlds. Our calculations span a range of planetary masses, core fractions, and orbital separations, showing that magnetic dissipation can substantially inflate radii and enhance mass-loss rates, especially in systems with large core-to-envelope ratios. These effects establish a coupled pathway of thermal inflation and erosion that naturally drives low-mass hot Saturns toward instability and strong enhancement in the loss of their H/He envelopes. The results suggest that magnetically induced heating is a key regulator of the close-in exoplanet population and may underlie the origin of the hot-Saturn desert.

1. INTRODUCTION

The physical diversity of close-in exoplanets reflects the competing effects of interior heat sources, stellar irradiation, and atmospheric escape. A planet's thermal evolution depends on how these energy reservoirs exchange and dissipate over time, regulating its radius, luminosity, and volatile retention. Tidal dissipation in eccentric orbits (Jackson et al. 2008; Ginzburg & Sari 2016) and misaligned orbits (Sethi & Millholland 2025) can inject substantial power into the deep interior, delaying thermal contraction on gaseous planets. Long-lived radiogenic decay and residual accretional heat likewise maintain intrinsic luminosity over gigayear timescales (Hubbard et al. 2002). In contrast, high-energy stellar radiation in the X-ray and extreme-ultraviolet (XUV; 1–912 Å) range impart energy in the upper atmosphere and can drive hydrodynamic escape of light gases (Lopez & Fortney 2013; Owen & Wu 2017; Gu & Chen 2023), removing substantial fractions of a planet's envelope and shaping the observed "radius valley."

Ohmic dissipation has emerged as a particularly compelling mechanism to explain the anomalously large radii of many close-in gas giants ("hot Jupiters"). In their seminal work, Batygin & Stevenson (2010) demonstrated that strong stellar irradiation drives ionized winds in a hot Jupiter's atmosphere, which, interacting with an imposed planetary magnetic field, induce currents that penetrate and heat the deep interior. Follow-up studies have mapped out how wind speed, conductivity profiles, and rotation modulate Ohmic power (Perna et al. 2010; Rauscher & Menou 2013; Wu & Lithwick 2013; Cohen et al. 2024) and have demonstrated correlations between incident flux and radius inflation across gas-giant populations (Ginzburg & Sari 2016; Thorngren & Fortney 2018). Others even suggest that Ohmic heating may play a role down to sub-Neptune masses, providing a continuous heating mechanism as planets transition from gas giants to smaller envelopes (Pu & Valencia 2017). More recently, Viganò et al. (2025) used Ohmically-heated evolutionary calculations to estimate the envelope wind intensities in order to reproduce the range of observed radii.

Planetary magnetic fields are central to the Ohmic paradigm, yet their strengths and geometries remain poorly constrained, especially for lower-mass objects. In the Solar System, Jupiter's dipole moment is roughly 10^5 times Earth's, while Saturn through Neptune exhibit weaker, more complex fields (Connerney et al. 2018). For exoplanets, dynamo-scaling laws tied to convective heat flux predict field strengths of order 1–100 G across gas giants and sub-

Corresponding author: Howard Chen
hchen@fit.edu

Table 1: Planetary Parameter Space and Key Model Assumptions

Quantity	Symbol	Values / Range	Units	Notes
Planet Mass	$M_{\rm p}$	60, 80, 100	$M_\oplus$	Core + envelope included
Orbital Separation	a	0.02, 0.04, 0.05	AU	Circular orbits assumed
Initial Envelope Fraction	$f_{\rm env}$	0.7, 0.8, 0.9	–	Fraction of $M_{\rm p}$ in H/He envelope
Stellar Age	$t_\star$	$10^{6.5}$–10^9	yr	Sampled logarithmically
Ohmic Heating	–	On / Off	–	Applied following standard scaling prescription (core)
Magnetic Field Strength	B	80–100	G	Assumed dipole surface field
Mass Loss Rate	$\dot{M}$	Computed	$M_\oplus$/yr	Energy-limited atmospheric escape
Planet Radius	$R_{\rm p}$	Computed	$R_\odot$	Converted to $R_{\rm J}$ where relevant
Equation of State	–	H/He EOS	–	Standard MESA implementation

Neptunes (Christensen et al. 2009; Reiners & Christensen 2010). Observational searches for radio emission or bow-shock signatures offer tantalizing but inconclusive hints (Vidotto et al. 2010; Hess & Zarka 2011).

Previous Ohmic-heating studies have typically prescribed planetary magnetic fields as fixed inputs rather than evolving them consistently with the planet's thermal and structural evolution. In reality, the field strength is set by convective luminosity and interior temperature gradients, quantities that Ohmic dissipation itself modifies, implying a time-dependent feedback between magnetic activity and energy deposition. This coupling is especially relevant for sub-Saturn and sub-Neptune planets, whose modest envelopes and diverse cooling histories can drive a wide range of dynamo behaviors. Here we incorporate a dynamo-scaling prescription directly into the Ohmic-heating framework, enabling more realistic predictions of radius inflation, magnetic observables, and long-term thermal evolution in the growing sample of hot Saturn-mass exoplanets. Here we calculate the interior Ohmic dissipation with an evolving dynamo in the hot-Saturn mass range, which is distinct from previous upper-atmosphere induction studies.

2. CALCULATIONS & NUMERICAL MODEL

In this study, we employed the stellar and planetary evolution code MESA (Modules for Experiments in Stellar Astrophysics; Paxton et al. 2010, 2013, 2015) to model the thermal evolution of exoplanets in the sub-Saturn mass range (approximately 60–100 $M_\oplus$). The MESA-planets suite 12778 version we used is based on previous work of Chen & Rogers (2016), Malsky & Rogers (2020), and Gu & Chen (2023). However, we turned off diffusive escape in our calculations here. Our models focused specifically on planets with hydrogen–helium (H/He) envelopes comprising between 1% and 10% of the total planetary mass. Equilibrium temperatures were chosen between 1300 K and 1500 K, motivated by previous findings that ohmic dissipation is most efficient within this temperature window; higher equilibrium temperatures typically result in negligible radius inflation for planets above Saturn mass, whereas lower temperatures significantly reduce heating efficiency (e.g., Batygin & Stevenson 2010; Pu & Valencia 2017).

Each planetary model is characterized by three primary parameters: planetary mass (fixed within each simulation), orbital separation, and envelope mass fraction (H/He ratio). Parameter ranges were guided by earlier modeling studies (Stevenson 1983; Kilmetis et al. 2024; Pu & Valencia 2017). Table 1 summarizes the range of planetary parameter space explored. The structural configuration in our MESA planet models consists of a well-defined core (either rocky or diffuse depending on the scenario considered) and an overlying gaseous envelope primarily composed of H and He, following standard assumptions employed widely in the literature.

2.1. *Magnetic Field & Ohmic Dissipation*

Here we couple planetary magnetic field evolution with Ohmic heating calculations in a self-consistent framework. Rather than prescribing the planetary magnetic field as an external parameter, we compute its strength internally at each timestep using dynamo-scaling relations that depend on the interior heat flux and convective luminosity. This approach captures the mutual feedback between magnetic activity and thermal evolution, yielding a more realistic estimate of radius inflation and long-term energy balance across the hot-Saturn parameter space.

We adopt the analytical dynamo-scaling relation of Kilmetis et al. (2024) (whom derived a scheme based on earlier works including Zhang & Rogers 2022; Reiners & Christensen 2010; Christensen et al. 2009) to evaluate the local magnetic field strength within the convective region:

$$B_{\rm dyn} = 0.68, f_{\rm ohm}, (F_{\rm conv,ref})^{2/3}, (\rho(z))^{1/3}, \tag{1}$$

where $f_{\rm ohm}$ is the Ohmic dissipation efficiency (taken as unity for the reference case), $F_{\rm conv,ref}$ is the convective energy flux, and $\rho(z)$ is the local density of the planetary gas envelope in $\rm kg\,m^{-3}$ The global dipole component emerging at the planetary surface is then given by

$$B_{\rm field} = \frac{B_{\rm dyn}}{\sqrt{2}} \left(\frac{R_p - R_{\rm end}}{R_p}\right)^3 \times 10^{-4}, \tag{2}$$

where R_p is the planetary radius and $R_{\rm end}$ marks the lower boundary of the dynamo-active shell how are these calculated).

The convective regime is characterized by the Reynolds number,

$$\mathrm{Re} = \frac{v_{\rm conv}(z), (R_{\rm start} - R_{\rm end})}{T(z)^{3/2}, (4\pi)}, \tag{3}$$

where $v_{\rm conv}(z)$ is the convective velocity evaluated between the inner core boundary ($R_{\rm start}$) and the outer convective limit ($R_{\rm end}$). The convective flux, which governs both energy transport and dynamo vigor, is expressed as

$$F_{\rm conv} = \frac{2, C_p(z), T(z), \rho(z)^2, v_{\rm conv}(z)^3}{-P(z), \left(\frac{d\ln\rho}{d\ln T}\middle| P\mathrm{gas}\right)}, \tag{4}$$

where $C_p(z)$ is the specific heat (is this directly from mesa or assumed), $T(z)$ the temperature, and $P(z)$ the pressure profile. The upper convective boundary, where $F_{\rm conv}$ approaches zero, defines the location of Ohmic power deposition.

Finally, the volumetric Ohmic heating rate is computed as

$$\dot{Q}_{\rm ohm} = \frac{B\mathrm{field}(T)^2, v_{\rm wind}^2, V_{\rm shell}}{\Delta m_{\rm conv}}, \tag{5}$$

where $v_{\rm wind}$ is the characteristic zonal wind speed (which we assume to be 1), $V_{\rm shell}$ the volume of the conducting region, and $\Delta m_{\rm conv}$ the mass of the convective shell. This formulation self-consistently couples the magnetic field strength, convective flux, and Ohmic power, allowing the model to evolve the planetary interior, radius, and mass-loss rate in tandem.

2.2. *Radiative-Recombination-, Energy-Limited Escape, & Core Heat*

In strongly irradiated regimes, the escape flow becomes hydrodynamic, driven by the combined stellar X-ray and EUV flux ($F_{\rm XUV}$) that deposits energy above the homopause and accelerates the upper atmosphere to transonic velocities (Tian et al. 2005; Murray-Clay et al. 2009). The XUV band spans roughly 1–912 Å, encompassing both the soft X-ray (1–100 Å) and extreme ultraviolet (100–912 Å) domains most effective at heating and ionizing the upper atmosphere. The absorbed high-energy flux sets the available power for escape, such that the energy-limited rate above implicitly scales with $F_{\rm XUV}$ rather than the bolometric flux. This coupling naturally captures the transition between weak, photon-limited loss and the full hydrodynamic outflow.

Here, atmospheric escape is incorporated through the standard energy-limited prescription (Watson et al. 1981; Lammer et al. 2003; Owen & Wu 2013), with the mass-loss rate:

$$\dot{M}_{\rm env} = -\frac{\varepsilon_{\rm EUV} \pi F_{\rm EUV} R_{\rm p} R_{\rm EUV}^2}{G M_{\rm p} K_{\rm tidal}}, \tag{6}$$

where $\varepsilon_{\rm EUV} = 0.1$ denotes the heating efficiency, $K_{\rm tidal}$ accounts for Roche-lobe effects, and $R_{\rm EUV}$ is the EUV absorption radius estimated from the photospheric scale height.

At high EUV fluxes ($F_{\rm EUV} \gtrsim 10^4$ erg s^{-1} cm^{-2}), the flow enters the radiation–recombination limited regime where photoionizations are balanced by radiative recombinations and Lyα cooling fixes the wind temperature near $T_{\rm wind} \sim 10^4$ K. In this regime, the energy-limited assumption breaks down and the mass-loss rate follows the expression of Murray-Clay et al. (2009):

$$\dot{M}_{\rm rr} = -\,\pi \left(\frac{GM_{\rm p}}{c_{\rm s}^2}\right)^2 \frac{c_{\rm s} m_{\rm H}}{} \left(\frac{F_{\rm EUV} G M_{\rm p}}{h\nu_0 \alpha_{\rm rec} R_{\rm EUV}^2 c_{\rm s}^2}\right)^{1/2} \exp\left[2 - \frac{GM_{\rm p}}{c_{\rm s}^2 R_{\rm EUV}}\right], \tag{7}$$

where $c_{\rm s} = (2k_{\rm B}T_{\rm wind}/m_{\rm H})^{1/2}$ is the isothermal sound speed and $\alpha_{\rm rec} = 2.7 \times 10^{-13}$ cm^3 s^{-1} is the hydrogen recombination coefficient at 10^4 K. At each timestep, the model evaluates both $\dot{M}_{\rm env}$ and $\dot{M}_{\rm rr}$, adopting the lesser of the two to ensure a continuous transition between the energy-limited and recombination-limited regimes:

The planetary core luminosity,

$$L_{\rm core} = -c_v M_{\rm core}\frac{dT_{\rm core}}{dt} + L_{\rm radio}, \tag{8}$$

is added as an internal energy source using composition-dependent specific heats and radionuclide decay terms (Guillot 2010; Schubert et al. 1980).

2.3. *Equation of State, Microphysics, and Interior Structure*

We evolve a spherically symmetric H/He envelope atop a heavy–element core using the Saumon–Chabrier–van Horn EOS (SCvH) for H/He, with fixed bulk composition ($Y = 0.25$, $Z = 0.03$ unless stated), and Rosseland-mean opacity tables from Freedman et al. (2014). The models employ a semi-grey atmospheric boundary condition based on the $T(\tau)$ relation of Guillot (2010), allowing the photospheric pressure to vary dynamically with optical depth rather than being fixed at a constant value. Radiative-convective transitions, irradiation, and envelope cooling are evolved self-consistently using MESA's `relax_irradiation` option, with initial conditions defined through a reinflation procedure that restores the target interior entropy prior to time integration. Core heating is included via a composition-dependent luminosity $L_{\rm core}$ (radioactive decay + thermal inertia) injected at the base of the envelope; the envelope may also receive distributed heating from Ohmic dissipation as described below.

The interior follows the standard 1-D structure system:

$$\frac{dm}{dr} = 4\pi r^2 \rho, \tag{9}$$
$$\frac{dP}{dr} = -\frac{Gm\rho}{r^2}, \tag{10}$$
$$\frac{dL}{dr} = 4\pi r^2 \rho \left(q_{\rm ohm} + q_{\rm radio} - T\,\frac{ds}{dt}\right), \tag{11}$$
$$\frac{dT}{dr} = \frac{T}{P}\,\nabla\,\frac{dP}{dr}, \qquad \nabla = \min(\nabla_{\rm rad},\, \nabla_{\rm ad})\,, \tag{12}$$

where $\rho(P,T)$ is supplied by the EOS, $q_{\rm ohm}$ is the volumetric Ohmic heating rate (zero in non-Ohmic runs), and $q_{\rm radio}$ captures any distributed radiogenic heating if present. The radiative temperature gradient is

$$\nabla_{\rm rad} \;=\; \frac{3\kappa L P}{64\pi\sigma G m T^4}, \tag{13}$$

with opacity $\kappa(P,T)$ from the tables, and σ the Stefan–Boltzmann constant; in convective zones we adopt the MESA default mixing-length treatment, so that $\nabla = \nabla_{\rm ad}$ where convection is efficient. Boundary conditions are set at the photosphere via the $T(\tau)$ relation and at the inner edge by the specified $L_{\rm core}$ and core radius.

Coupling to magnetic/Ohmic heating.—The Ohmic source term $q_{\rm ohm}$ in Eq. (11) is supplied by our dynamo-linked prescription: a convective-flux–based field $B_{\rm dyn}$ is mapped to the surface dipole $B_{\rm field}$ and converted to volumetric heating $\dot{Q}_{\rm ohm}$ within the conducting shell; numerically, $q_{\rm ohm} \equiv \dot{Q}_{\rm ohm}/(4\pi r^2 \rho)$ and is added to MESA's energy equation while the structure iterates to equalibrium.

3. RESULTS

Figure 1 presents the temporal evolution of hydrodynamic mass-loss rates for planets of 60 and 80, $M_\oplus$ subject to varying orbital separations and envelope mass fractions. In both mass regimes, escape rates peak at $\dot{M}$env $\sim 10^{12}$–$10^{13}, M\oplus, {\rm yr}^{-1}$ during the early EUV-saturated phase of stellar evolution, followed by a monotonic decline as the planets cool and contract. For the 60, $M_\oplus$ models (Fig. 1a), closer orbital distances and more massive envelopes sustain enhanced escape over extended intervals, whereas tenuous envelopes rapidly approach asymptotically low loss rates. The 80, $M_\oplus$ models (Fig. 1b) exhibit a similar decrease, though the sensitivity to envelope fraction is reduced

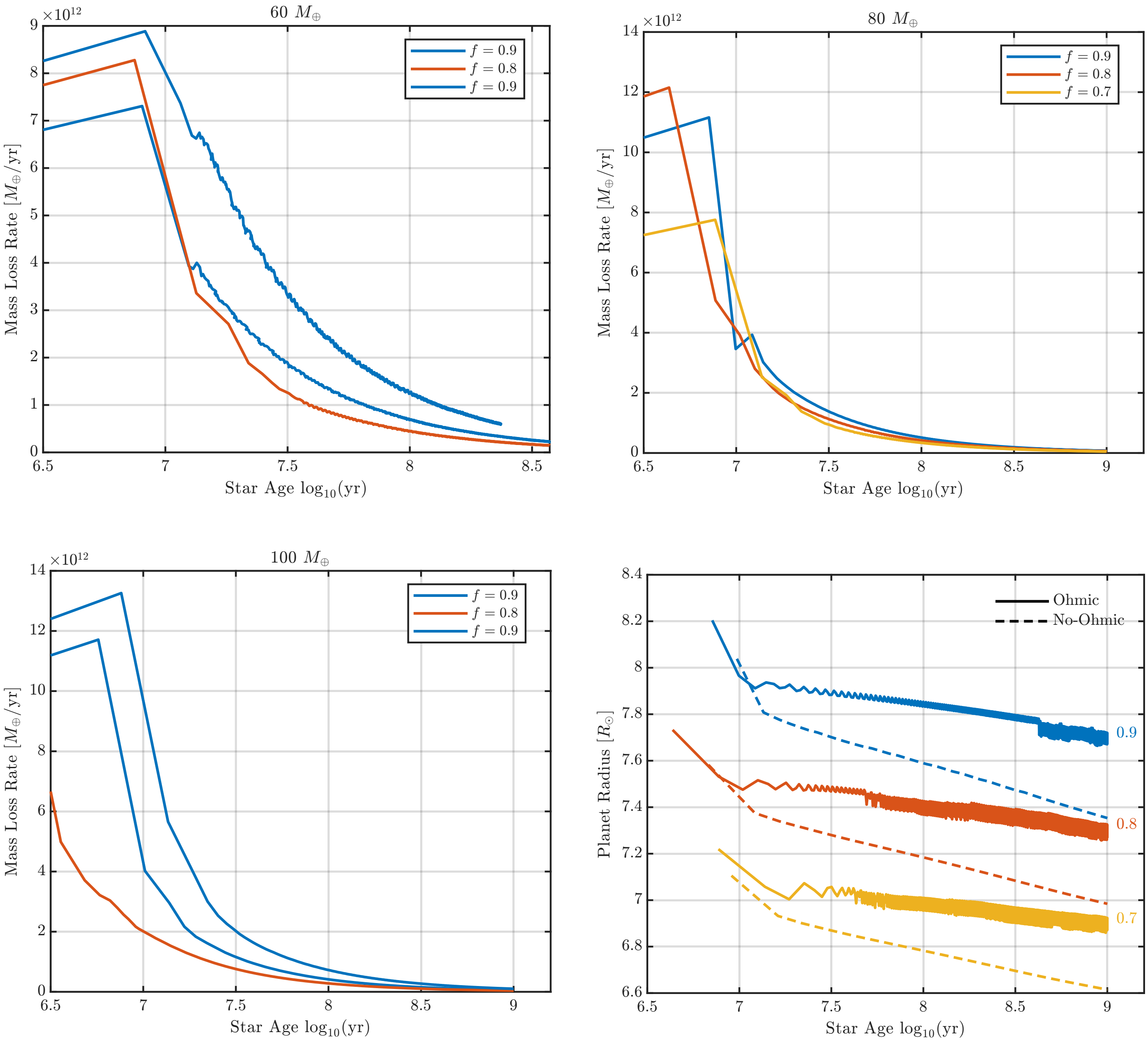

Figure 1: Time evolution of atmospheric escape and radius contraction for hot Saturns. **(a)** $60\,M_\oplus$ planets at two orbital separations and varying envelope fractions. **(b)** $80\,M_\oplus$ planets at $a = 0.05$ AU with envelope fractions $f = 0.9, 0.8, 0.7$. **(c)** $100\,M_\oplus$ planets at $a = 0.05$ AU with varying envelope fractions. **(d)** Radius evolution with (solid) and without (dashed) Ohmic heating, showing sustained inflation across a range of envelope fractions. Across all masses, mass-loss rates peak early (10^{12}˘$10^{13}\,M_\oplus\,\mathrm{yr}^{-1}$) during the EUV-luminous phase of the star and then decline as the planets cool and contract. Lower-mass planets and higher envelope fractions experience the most extended mass-loss histories, while Ohmic heating maintains significantly larger radii compared to non-Ohmic cases, highlighting the feedback between magnetic dissipation, escape, and structural evolution.

as the mass-loss rates converge by $\sim 10^8$, yr. These results demonstrate that both total mass and envelope fraction, through their influence on the magnetic field strengths and the power of Ohmic heating, modulate the early and long-term atmospheric escape.

For the 100, $M_\oplus$ cases (Fig. 1c), the overall trend is similar to the lower-mass models: mass-loss rates peak early, near 10^{12}–10^{13}, $M_\oplus$, yr^{-1}, and then decline as the planets contract and the stellar EUV flux decreases. However, the higher planetary mass stabilizes the envelope, producing faster convergence across different initial envelope fractions, and by late times the mass-loss rates are nearly indistinguishable. Panel (d) highlights the impact of Ohmic dissipation on radius evolution: planets with Ohmic heating remain more inflated than their non-Ohmic counterparts, with differences of several tenths of a Jupiter radius persisting well into Gyr timescales. This sustained inflation, despite ongoing mass loss, underscores the role of magnetically induced heating as a counteracting process to standard cooling and contraction, particularly for planets with large initial H/He envelopes. Selected results are also summarized in Table 2.

Table 2: Ohmic heating, mass-loss rate, and magnetic field for varying orbital separations of 80 and 60 $M_\oplus$ planets.

Sep (AU)	Age (log[Gyr])	$P_{\rm ohm}$ (W)	$\dot{M}$ ($M_\oplus$ yr^{-1})	B (G)
		80 $M_\oplus$		
0.05	6.8	5.46×10^{17}	1.12×10^{13}	9.50×10^{1}
0.05	7.0	4.25×10^{17}	3.46×10^{12}	1.02×10^{2}
0.05	8.0	2.73×10^{17}	5.13×10^{11}	1.02×10^{2}
0.04	6.7	6.79×10^{17}	1.65×10^{13}	9.43×10^{1}
0.04	7.0	3.47×10^{17}	6.78×10^{12}	1.03×10^{2}
0.04	8.0	3.35×10^{17}	9.03×10^{11}	1.00×10^{2}
0.02	6.0	6.61×10^{17}	4.11×10^{13}	9.79×10^{1}
0.02	7.0	6.62×10^{17}	1.45×10^{13}	9.74×10^{1}
0.02	8.0	3.33×10^{17}	5.29×10^{12}	9.55×10^{1}
		60 $M_\oplus$		
0.05	6.9	5.30×10^{17}	7.31×10^{12}	8.69×10^{1}
0.05	7.0	3.79×10^{17}	4.75×10^{12}	9.48×10^{1}
0.05	8.0	2.40×10^{17}	6.94×10^{11}	9.38×10^{1}
0.04	6.9	6.60×10^{17}	8.89×10^{12}	8.64×10^{1}
0.04	7.0	4.61×10^{17}	7.37×10^{12}	9.35×10^{1}
0.04	8.0	2.98×10^{17}	1.27×10^{12}	9.26×10^{1}
0.02	6.0	5.82×10^{17}	4.88×10^{13}	9.12×10^{1}
0.02	7.0	5.89×10^{17}	1.69×10^{13}	9.12×10^{1}
0.02	8.0	5.89×10^{17}	8.02×10^{12}	8.99×10^{1}

Figure 2 shows the mass-loss rates for 60–100 $M_\oplus$ planets at orbital separations of 0.02–0.05 AU, comparing simulations with and without Ohmic heating. In all cases, the non-Ohmic models (dashed curves) follow the expected monotonic decline in escape rate as the envelopes cool and contract, tracing a nearly linear relationship between radius and mass-loss rate. The inclusion of Ohmic dissipation (solid curves) produces a pronounced departure from this trend: magnetic energy deposited in the deep interior inflates planetary radii and elevates atmospheric escape by roughly one to two orders of magnitude. This amplification is most prominent for the 60 $M_\oplus$ cases, where sustained Ohmic power maintains inflated radii long after the stellar EUV flux declines, but remains evident across the entire Saturn-mass regime.

These results demonstrate that Ohmic heating introduces a feedback loop between magnetic dissipation, thermal expansion, and hydrodynamic escape. As the envelope inflates, the enhanced wind–field coupling strengthens interior currents, reinforcing both radius inflation and mass loss over Gyr timescales. The persistence of large radii despite significant atmospheric depletion is consistent with the exponential inflation mechanism proposed by Pu & Valencia (2017), highlighting the role of magnetic heating as a long-lived regulator of the evolution of hot exoplanets.

The final outcomes of our models, summarized in Figure 3, reveal a non-linear dependence of magnetic field strength[1], Ohmic heating efficiency, and late-time mass-loss rates on orbital separation across the 60–100 $M_\oplus$ regime. Panel (a) shows that magnetic dipole strengths generally increase with decreasing orbital distance, but with a pronounced

[1] The magnetic field strengths quoted in this work represent the local dynamo-generated fields within the convective interior, as derived from the scaling relations of Christensen et al. (2009) and Reiners & Christensen (2010). These values should not be directly compared to the surface dipole moments inferred for Solar System planets, which are typically one to two orders of magnitude weaker due to geometric attenuation and field topology.

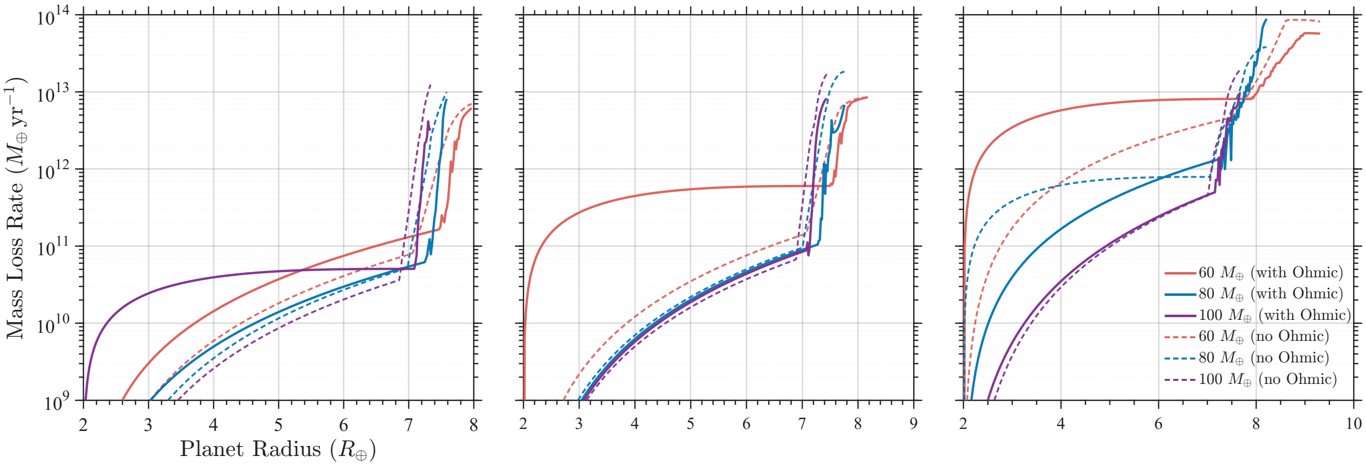

Figure 2: Coupled evolution of radius inflation and atmospheric escape for 60, 80, and 100 $M_\oplus$ hot Saturns with (solid) and without (dashed) Ohmic heating. Each panel corresponds to a different orbital separation: *top-left* — 0.02 AU, *top-right* — 0.04 AU, and *bottom* — 0.05 AU. In all cases, magnetic dissipation inflates planetary radii and enhances mass-loss rates by up to one to two orders of magnitude relative to non-Ohmic models, consistent with the exponential inflation mechanism proposed by Pu & Valencia (2017). The persistence of inflated radii even as the planets cool and contract illustrates the self-reinforcing coupling between magnetic dissipation, thermal structure, and hydrodynamic escape, particularly within the sub-Saturn mass regime where Ohmic heating remains energetically significant.

maximum near 0.04 AU for the $60\,M_\oplus$ case. This peak reflects the balance between vigorous convective fluxes, which favor dynamo activity, and the onset of rapid mass loss, which subsequently depletes the envelope and damps the dynamo. Because faster cooling enhances the intrinsic luminosity, lower-mass planets initially sustain stronger convective fluxes and thus stronger magnetic fields. Higher-mass planets, by contrast, cool more slowly and exhibit more muted variations, converging toward $\sim$ 90–100 G fields that are relatively insensitive to separation. Similarly, the Ohmic heating power in panel (b) rises sharply for close-in, lower-mass planets, reaching $\gtrsim 10^{18}$ W at 0.04 AU for the $60\,M_\oplus$ models, while the $100\,M_\oplus$ cases remain an order of magnitude lower. (mention some implication here)

The late-time mass-loss rates (Fig. 1c) show the enhanced susceptibility of lower-mass planets to total erosion. At $a = 0.02$ AU, the $60, M_\oplus$ models sustain $\dot{M}\mathrm{env} \sim 10^{13}, M\oplus, \mathrm{yr}^{-1}$, whereas the 80 and $100, M_\oplus$ cases decline to $\sim 10^{12}, M_\oplus, \mathrm{yr}^{-1}$. Beyond $\sim$ 0.04 AU, all models exhibit sharply attenuated escape consistent with the radial decay of stellar EUV irradiation. The results indicate that Ohmic dissipation and dynamo-driven heating jointly destabilize the envelopes of close-in, low-mass hot Saturns, while more massive analogs remain thermally buffered against runaway inflation and escape. The coupling between magnetic energy deposition, envelope expansion, and hydrodynamic outflow is therefore expected to peak in the sub-Saturn regime, producing the strongest deviations from standard cooling–contraction evolution.

4. DISCUSSION

In this study, we have demonstrated that Ohmic heating, when modeled self-consistently with planetary magnetic field evolution, can substantially alter the thermal and mass-loss histories of hot Saturn-mass planets. By linking dynamo scaling with interior luminosity and convective flux, our models capture a time-dependent feedback in which magnetic fields regulate Ohmic dissipation and, in turn, are influenced by the altered thermal structure. We find that lower-mass ($\sim$60–80 $M_\oplus$) hot Saturns are particularly susceptible to runaway inflation and hydrodynamic escape, with heating powers exceeding 10^{18} W and late-time mass-loss rates several orders of magnitude above cooling-only predictions. Higher-mass cases ($\sim$100 $M_\oplus$) remain more resilient, converging toward modest inflation and suppressed escape. These results demonstrate the importance of including magnetic dissipation in evolutionary models of hot gaseous exoplanets.

Our findings build on earlier work that invoked Ohmic heating to explain radius anomalies in hot Jupiters (e.g., Batygin & Stevenson 2010; Wu & Lithwick 2013; Perna et al. 2010) and extended it into the sub-Saturn regime (Pu & Valencia 2017). While prior studies typically prescribed static field strengths, our approach explicitly evolves the dynamo, showing how faster cooling in lower-mass planets produces stronger convective fluxes and initially stronger fields. This helps to explain why Ohmic dissipation can be disproportionately efficient in sub-Saturns, a feature not

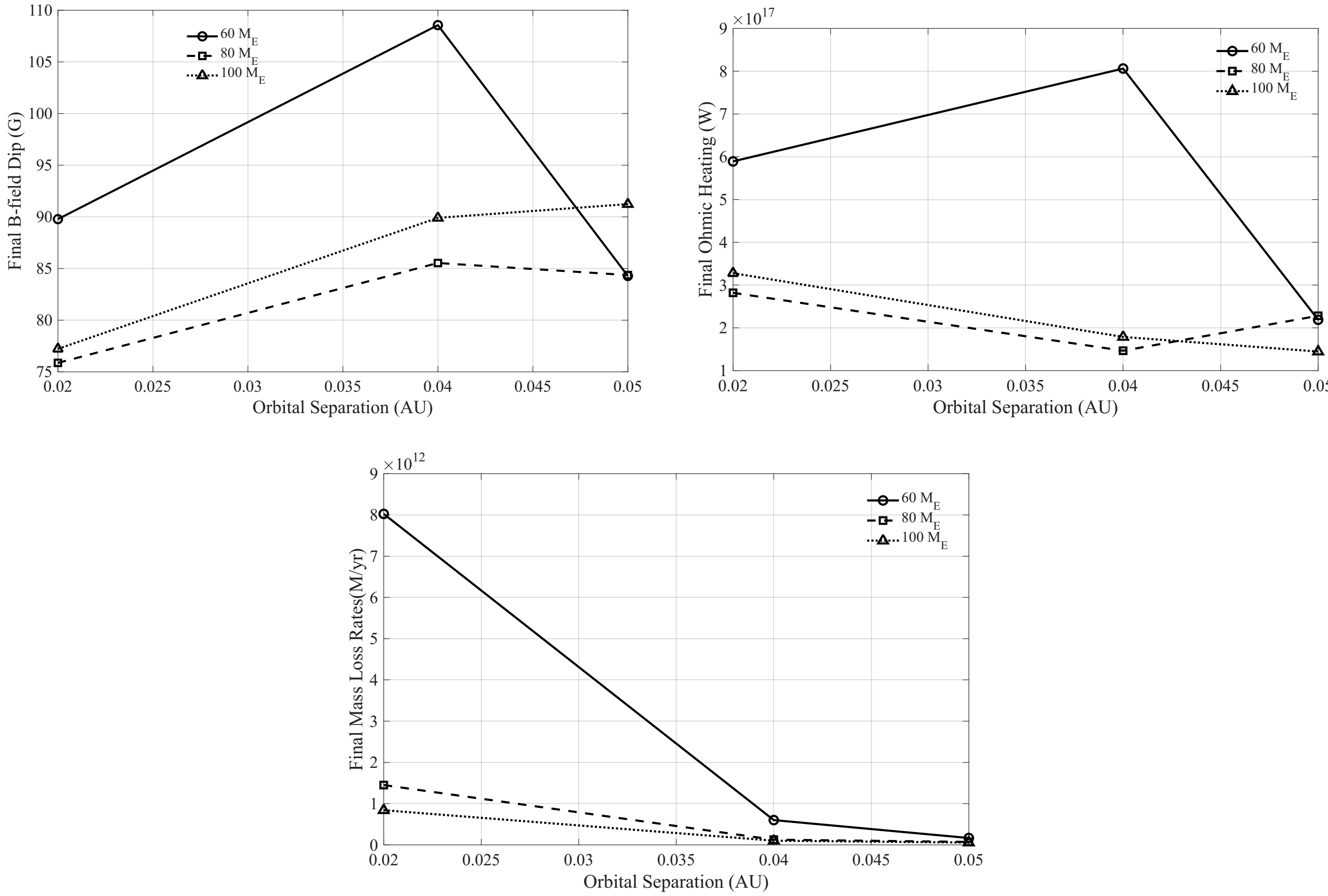

Figure 3: Final planetary properties after coupled evolution with self-consistent magnetic field growth, Ohmic heating, and atmospheric mass loss, shown as a function of orbital separation. From left to right: (a) magnetic dipole strength, (b) radius inflation relative to non-Ohmic models, and (c) late-time mass-loss rates. Different line styles denote planetary masses (60–100 $M_\oplus$). The results highlight how lower-mass planets at small separations sustain stronger fields, enhanced Ohmic dissipation, and larger escape rates, whereas higher-mass analogs converge to weaker evolutionary responses.

captured by fixed-field treatments. Our models also align with recent dynamo-scaling predictions (e.g., Christensen et al. 2009; Kilmetis et al. 2024) that suggest a strong mass dependence in field strength, though here we show how this directly translates into divergent thermal and mass-loss pathways.

Recent studies have quantified Ohmic heating produced in upper atmospheres by time-varying external magnetic fields, with applications to small/rocky-to-sub-Neptune planets such as TRAPPIST-1 b and π Men c, and have shown that ionospheric heating can be strong and may even compete with XUV under certain conditions (Strugarek et al. 2025). Here, we model deep-interior Ohmic dissipation driven by winds shearing a planetary magnetic field whose strength co-evolves with the planet's thermal and convective state. We apply this framework to hot Saturn-mass planets (60–100 $M_\oplus$) coupling dynamo scaling to interior evolution and mass loss. In this regime, the interior energy budget and radius evolution dominate the observable outcomes, and we find that Ohmic heating substantially amplifies escape and inflation for lower-mass hot Saturns.

Our theoretical predictions can be probed with both current and upcoming surveys. Inflated radii persisting into Gyr ages should manifest as outliers in the mass–radius distribution of Saturn-mass exoplanets, a signal accessible to TESS, CHEOPS, and PLATO transit samples. Atmospheric escape enhanced by Ohmic inflation could be detectable via excess Lyα or He 1083 nm absorption, as demonstrated in recent escape detections. Finally, strong magnetic fields implied by our models may be probed indirectly via radio auroral emission or bow-shock asymmetries in transit light curves (Vidotto et al. 2010, 2019; Hess et al. 2014), though such signatures remain observationally challenging. The combination of structural inflation, spectral escape tracers, and magnetospheric diagnostics offers a multi-pronged way to test our framework.

In younger systems, additional effects may modulate Ohmic heating. Gas drag from residual protoplanetary disks could enhance angular momentum loss and regulate the early spin states that influence wind-driven currents. At the same time, elevated accretion luminosities and hotter interiors during the first 100 Myr provide the largest convective fluxes, potentially driving stronger dynamos than at later times. These considerations suggest that Ohmic dissipation may be most dramatic in young, still-cooling sub-Saturns, aligning with the expectation that mass loss is also most vigorous in the early EUV-luminous epoch of the host star. Observations of systems such as GW Ori, with multi-planet gas-rich environments, could provide critical constraints on this early-time coupling.

Although the detailed dependence of magnetic field strength and Ohmic power on orbital separation is non-linear, the combined effect is that lower-mass hot Saturns experience the strongest heating and the highest mass-loss rates, making them the most vulnerable to runaway inflation and atmospheric escape. This instability provides a natural pathway toward explaining the dearth of low-mass close-in Saturns—the so-called "hot-Saturn desert." By contrast, higher-mass analogs remain buffered against runaway outcomes, helping to explain the population-level asymmetry seen between sub-Saturns and more massive hot Jupiters.

Future work should expand these calculations to account for additional processes and broader parameter ranges. A natural extension is to include tidal dissipation and eccentricity pumping (e.g., Jackson et al. 2016; Louden et al. 2023; Batygin 2025), which may work alongside with Ohmic heating to prolong inflation phases. Exploring a wider range of envelope metallicities and conductivity profiles will further constrain how core composition shapes current penetration and magnetic feedback. Combining improved interior-evolution models (e.g., Tang et al. 2025) with coupled photochemistry and radiative transfer will allow direct comparisons to JWST spectra of warm and hot Saturns.

5. CONCLUSION

Our simulations reveal that Ohmic dissipation, when implemented self-consistently to planetary dynamo evolution, profoundly alters the thermal and mass-loss histories of hot Saturn-mass exoplanets. Lower-mass ($\sim 60 - 80 M_{\oplus}$) planets exhibit runaway inflation and enhanced atmospheric escape, with Ohmic heating powers exceeding 10^{18} W and mass-loss rates up to several orders of magnitude above standard thermal contraction models without dissipative effects. In this regime, higher-mass ($\sim 100\ M_{\oplus}$) analogs in contrast remain comparatively stable, underscoring a strong mass dependence in magnetic–thermal coupling.

Our results demonstrate that magnetic dissipation plays a central role in the coupled thermal and mass-loss evolution of sub-Saturns. Self-consistent treatment of dynamo activity and Ohmic heating reveals a feedback that drives rapid atmospheric erosion in low-mass planets while sustaining inflated radii. Ours result indicate that importantly, Ohmic heating cannot be treated as a minor correction to energy balance, but rather as a dominant process shaping the observable radii and escape histories of hot Saturns.

5.1. *Data & Code Availability*

The data supporting the plots and findings of this study are available from the corresponding author upon request. The most up-to-date version of the code used in this study will be made available upon request and upon publication of the work.

H.C. acknowledges the AI.panther computational facility at Florida Tech, supported by the National Science Foundation MRI Award No. 2016818 (project title: "Acquisition of a High Performance GPU/CPU Cluster for Research and Innovation in Computational Sciences and Engineering").

REFERENCES

Batygin, K. 2025, The Astrophysical Journal, 985, 87

Batygin, K., & Stevenson, D. J. 2010, The Astrophysical Journal Letters, 714, L238

Chen, H., & Rogers, L. A. 2016, The Astrophysical Journal, 831, 180

Christensen, U. R., Holzwarth, V., & Reiners, A. 2009, Nature, 457, 167

Cohen, M., Palmer, P. I., Paradise, A., Bollasina, M. A., & Tiranti, P. I. 2024, The Astronomical Journal, 167, 97

Connerney, J. E. P., Yelle, R. V., & Waite, J. H. 2018, Journal of Geophysical Research: Space Physics, 123, 27

Freedman, R. S., Lustig-Yaeger, J., Fortney, J. J., et al. 2014, The Astrophysical Journal Supplement Series, 214, doi:10.1088/0067-0049/214/2/25

Ginzburg, S., & Sari, R. 2016, The Astrophysical Journal, 819, 116

Gu, P.-G., & Chen, H. 2023, The Astrophysical Journal Letters, 953, L27

Guillot, T. 2010, Astronomy and Astrophysics, 520, A27

Hess, S. L., Echer, E., Zarka, P., Lamy, L., & Delamere, P. 2014, Planetary and Space Science, 99, 136

Hess, S. L. G., & Zarka, P. 2011, Astronomy Astrophysics, 531, A29

Hubbard, W. B., Burrows, A., & Lunine, J. I. 2002, Annual Review of Astronomy and Astrophysics, 40, 103

Jackson, B., Barnes, R., & Greenberg, R. 2008, The Astrophysical Journal, 681, 1631

Jackson, B., Jensen, E., Peacock, S., Arras, P., & Penev, K. 2016, Celestial Mechanics and Dynamical Astronomy, 126, 227

Kilmetis, K., Vidotto, A. A., Allan, A., & Kubyshkina, D. 2024, Monthly Notices of the Royal Astronomical Society, 535, 3646

Lammer, H., Selsis, F., Ribas, I., et al. 2003, The Astrophysical Journal, 598, L121

Lopez, E. D., & Fortney, J. J. 2013, The Astrophysical Journal, 776, 2

Louden, E. M., Laughlin, G. P., & Millholland, S. C. 2023, The Astrophysical Journal Letters, 958, L21

Malsky, I., & Rogers, L. A. 2020, The Astrophysical Journal, 896, 48

Murray-Clay, R. A., Chiang, E. I., & Murray, N. 2009, The Astrophysical Journal, 693, 23

Owen, J. E., & Wu, Y. 2013, The Astrophysical Journal, 775, 105

—. 2017, The Astrophysical Journal, 847, 29

Paxton, B., Bildsten, L., Dotter, A., et al. 2010, The Astrophysical Journal Supplement Series, 192, 3

Paxton, B., Cantiello, M., Arras, P., et al. 2013, The Astrophysical Journal Supplement Series, 208, 4

Paxton, B., Marchant, P., Schwab, J., et al. 2015, The Astrophysical Journal Supplement Series, 220, 15

Perna, R., Heng, K., & Pont, F. 2010, The Astrophysical Journal, 719, 1421

Pu, B., & Valencia, D. 2017, The Astrophysical Journal, 835, 43

Rauscher, E., & Menou, K. 2013, The Astrophysical Journal, 764, 103

Reiners, A., & Christensen, U. R. 2010, Astronomy & Astrophysics, 522, A13

Schubert, G., Stevenson, D., & Cassen, P. 1980, Journal of Geophysical Research: Solid Earth, 85, 2531

Sethi, R., & Millholland, S. C. 2025, The Astrophysical Journal, 988, 247

Stevenson, D. 1983, Reports on Progress in Physics, 46, 555

Strugarek, A., Muñoz, A. G., Brun, A., & Paul, A. 2025, Astronomy & Astrophysics, 693, A220

Tang, Y., Fortney, J. J., Nimmo, F., et al. 2025, The Astrophysical Journal, 989, 28

Thorngren, D. P., & Fortney, J. J. 2018, The Astronomical Journal, 155, 214

Tian, F., Toon, O. B., Pavlov, A. A., & De Sterck, H. 2005, The Astrophysical Journal, 621, 1049

Vidotto, A., Feeney, N., & Groh, J. 2019, Monthly Notices of the Royal Astronomical Society, 488, 633

Vidotto, A. A., Jardine, M., & Helling, C. 2010, The Astrophysical Journal Letters, 722, L168

Viganò, D., Sengupta, S., Soriano-Guerrero, C., et al. 2025, Astronomy & Astrophysics, 701, A8

Watson, A. J., Donahue, T. M., & Walker, J. C. 1981, Icarus, 48, 150

Wu, Y., & Lithwick, Y. 2013, The Astrophysical Journal, 772, 74

Zhang, J., & Rogers, L. A. 2022, The Astrophysical Journal, 938, 131